Intrinsic charge trapping and reversible charge induced structural modifications in a-Si3N4

Hückmann, L.; Cottom, J.P.; Meyer, J.

ADVANCED PHYSICS RESEARCH Open Access
www.advphysicsres.com

Intrinsic Charge Trapping and Reversible Charge Induced Structural Modifications in a-Si_3N_4

Lukas Hückmann, Jonathon Cottom, and Jörg Meyer**

Amorphous silicon nitride (a-Si_3N_4) is an essential material for a wide variety of electronic devices, ranging from its use in dielectric layers to its paramount importance for memory applications. In particular, the latter has triggered the interest in charge trapping, for which so-called N- and K-centers have been identified in experiments – with the atomistic configuration still subject of vigorous debate. Here, the range of hole and electron traps in stoichiometric a-Si_3N_4 are revealed by combining atomistic calculations at different levels of theory. The variety of sites within the amorphous network are characterized by introducing a statistical sampling method to quantify the statistical completeness of structural models obtained from a melt-quench procedure, in combination with a powerful local descriptor inspired by Tolman's angle. Hole trapping is dominated by two-coordinate N-centers, resulting in shallow hole traps. In contrast, electron trapping exhibits more nuanced behavior, encompassing both intrinsic polaronic trapping and the previously identified K-center type trapping (silicon dangling bond *SiN_3). Intrinsic polaronic trapping originates from distorted SiN_4 tetrahedra. Structural relaxation of the intrinsic polaron sites results in significant elongation of a Si-N bond and reversible generation of *SiN_3 and N_3Si-$SiN_{x \in \{3,4\}}$ defects.

1. Introduction

Amorphous silicon nitride (a-Si_3N_4) is an essential material for nanoelectronics due to its excellent mechanical and electrical properties.[1] Its hardness, resistance to chemicals and irradiation, and low permeability make it widely used as a protective layer in MEMS, photovoltaics, and semiconductor chip production.[2–4] Exceptional among the many properties of a-Si_3N_4 is the ability to trap charges stably and reversibly over the long term (approximately 10 years at 150 °C).[5,6] As such, it is employed in modern non-volatile charge-trap memory devices. Generally speaking, these devices operate via electrons tunneling through a floating gate material by applying an electric field and getting trapped in the underlying a-Si_3N_4. The associated trap states are spatially localized and immobile, which allows data to be stored with good retention characteristics even when the device is turned off.[1,7–14]

The origin of the charge trapping and the associated memory effect in a-Si_3N_4 has been the subject of intense study and debate for the last 56 years since the phenomena were first identified.[15,16] Robertson and others identified the so-called K- and N-centers as important defect centers in a-Si_3N_4, with the K-center responsible for the memory effect.[17–21] Electron paramagnetic resonance (EPR) measurements provided further insights into the local environment of both the K- and N-centers. The K-centers were found to be localized on Si, with the simplest model involving a Si-dangling bond, whereas the N-center was attributed to the two-coordinated N-atoms.[21–26] Both the N- and K-centers show negative-U behavior where the negative/positive charge state is favored with respect to the neutral ($2N^0/2K^0 \rightarrow N^-/K^- + N^+/K^+$).[24,27] The attribution of the N-center to undercoordinated N-sites is generally agreed upon; however, an appropriate atomistic model for the memory-active K-center is still debated. The challenge is compounded by the structural complexity inherent in amorphous and disordered thin films resulting in a wide range of potential defect environments giving rise to dramatically different trapping behaviors.

Characterizing a-Si_3N_4 is challenging as with all non-glass forming thin films, the amorphous phase is only stable as a strain-stabilized thin film with a significant substrate dependence on the morphology and associated properties.[28–33] This gives rise to a wide range of reported properties that depend both on the substrate and the deposition method. Reported densities vary between $\rho_a = 2.6$ to 3.2 g cm^{-3} (ground state crystal reference β-$Si_3N_4 = 3.2$ g cm^{-3}) with bulk modulus 150 to 210 GPa (β-$Si_3N_4 = 263$ GPa). The same trends are observed in the electronic properties with a broad range of literature band gaps between 3.1 to 6.0 eV, with values of 4.2 to 5.4 eV typically reported

L. Hückmann, J. Cottom, J. Meyer
Leiden Institute of Chemistry
Gorlaeus Laboratories
Leiden University
P.O. Box 9502, Leiden 2300 RA, The Netherlands
E-mail: l.huckmann@lic.leidenuniv.nl; j.meyer@chem.leidenuniv.nl

The ORCID identification number(s) for the author(s) of this article can be found under https://doi.org/10.1002/apxr.202300109

DOI: 10.1002/apxr.202300109

(β-Si_3N_4 = 6.2 eV).[19,31,32,34–36] The combination of a broad range of properties dictated by substrate and deposition method, along with inherent averaging effects in the measurements means care must be taken in interpreting the a-Si_3N_4 structures.

To understand the structural complexities inherent in a-Si_3N_4, modeling studies have played a vital role since the earliest days. The structural models are typically produced using either classical or ab initio molecular dynamics via a melt-quench procedure.[37–41] This approach was conceived to mimic the formation of glass-forming materials (typically SiO_2) and while not strictly a mimic of formation for a-Si_3N_4, the structures produced match well with the available experimental data.[28–30] Both approaches, classical and ab initio, produce comparable structures for stoichiometric a-Si_3N_4. Where defects are introduced into the melt or sub-stoichiometry is considered ab initio approaches are more common as they can be used without the need for reparameterizing a potential (the trade-off for this general applicability is computational time and limited supercell size).[37,39,41–44] However, it is important to note both approaches have been successfully deployed in all of the highlighted use cases producing results that accord well with experimentally characterized a-Si_3N_4.

The structural modeling has been complemented by defect studies utilizing periodic and cluster models of both the crystalline and amorphous Si_3N_4.[39,45–48] These studies have been motivated by the need to gain a more complete understanding of the charge trapping in a-Si_3N_4. The ultimate objective is an unambiguously agreed-upon atomistic model of the centers responsible for the memory effect. Through a combination of theory and experiment, two main candidates have emerged as the charge trapping memory (CTM) active center. With trapping either at a Si-dangling bond (most commonly referred to as the K-center) or on a Si-Si bond. These form a single defect in the crystal calculations as both motifs are found in the nitrogen vacancy (V_N). The calculated trapping levels show good agreement with the experimental trap levels in the bandgap of $\approx\pm$1.4 eV[49,50] above valance and below the conduction band edges, respectively.[38–40,46,50–52] The assignment is further bolstered by experimental studies that show enhanced trapping in Si-rich regions of a-Si_3N_4.[51,53] It is important to acknowledge that while disagreements may persist on the exact nature of the CTM active trap, two closely related candidate defects have been identified. Indeed, the Si-Si defect at large Si-Si distances can be viewed as two Si dangling bonds as the correlation between centers decreases to zero and vice versa.

The phenomenon of intrinsic electron and hole trapping is well-known in a wide range of amorphous inorganic oxides and beyond.[54–61] In all cases, the trapping is polaronic in nature and driven by a degree of localization at the band edges as a result of varying local environments.[62] These partially localized or Anderson states[63] can lead to a dramatic increase in the polaron (and bi-polaron) trapping energies. As our understanding of this phenomenon has evolved, it has been found in various materials and is now known to play an important role in the leakage and breakdown of a range of amorphous oxides.[58,62] Similar polaronic trapping has yet to be identified in amorphous nitride films; however, a-Si_3N_4 shows a range of traps distinct from the memory active sites discussed above, with trapping energies and concentrations similar to those identified in oxides.[17,57,64,65] How these hitherto unidentified trap states compare with the desired memory active centers and whether they contribute to the observed lateral leakage is an open question. Insights in this direction would allow the optimization of a-Si_3N_4 layer to both maximize the accessible trap density while reducing (ideally eliminating) lateral leakage.

In this article, we provide new insights into charge trapping in stoichiometric a-Si_3N_4 and its relation to structural features at the atomic scale by combining atomistic calculations at different levels of theory. To do so, we introduce a statistical sampling approach for amorphous systems to quantify how a given structural descriptor converges as a function of sample size, thereby allowing an appropriate number of samples to be selected. In addition, a novel site-centered descriptor inspired by Tolman's angle is introduced to aid the analysis and characterization of the local geometry. These models are then utilized to explore the intrinsic trapping of electrons and holes in a-Si_3N_4. The identified trapping centers are geometrically categorized, and the link to trapping energy is demonstrated. From this analysis, a description of the trapping precursor sites is extracted and linked to the structure. Finally, the interplay between the intrinsic electron traps and the reversible and irreversible modifications to the amorphous network are described in the context of breakdown and leakage.

2. Methods

2.1. Computational Details

A two-stage model-building approach was employed utilizing classical molecular dynamics to produce the initial amorphous structures, with the MD geometries revised and the electronic structure calculated with density functional theory (DFT). The MG2 potential and the LAMMPS[66] code were selected to generate the initial models via a classical MD melt-quench procedure applied to periodic 280 atom cells of β-Si_3N_4. The MG2 potential was selected as it had previously been demonstrated to produce structural models that accord well with the experimentally characterized films.[41,42,67] A range of box sizes (112, 280, 336, 672, and 1512) and cooling rates (0.1, 1, 10 K ps^{-1}) were tested to ensure any size and cooling rate effects were understood and the boxes taken to production were free of such artifacts. The full results of the box size and cooling rate convergence tests are included in the Supporting Information; the only point of note was a large structural instability was observed in the smallest boxes containing 112 atoms - a size that had been used for fully DFT-based simulations before.[39,68] The MQ was performed using a simulation time step of 0.5 fs. The Nosé-Hoover thermostat and barostat[69–71] were applied to control the *NpT* conditions with coupling constants set to the hundred- and thousandfold of the simulation time step. Ring statistics were performed with the RINGS software package[72] employing the primitive rings algorithm[73,74] and a cut-off of $r = 2.25$ Å. An initial ensemble size of 300 boxes was converged based upon the sampling methodology outline in Section 2.2; upon hybrid-DFT optimization the sample size was further reduced to 100 boxes.

The DFT calculations were performed spin-polarized using CP2K[75] with the DZVP-SR-MOLOPT[76] family of basis-sets to describe the valence electrons, and the GTH pseudopotentials[77,78] to describe the core electrons. An energy cutoff of 650 Ry and a relative cut off of 70 Ry was used to achieve

an initial convergence of 0.1 meV per formula unit, including only the Γ-point for Brillouin zone sampling in the simulation cells containing 280 atoms. The lattice vectors and ion positions were relaxed using the quasi-Newton BFGS update scheme. The convergence criteria was 10^{-7} eV and 0.005 eV Å^{-1} for forces. An initial pre-optimization with the PBE[79,80] functional was performed to provide an improved initial guess for the wave function (and geometries), followed by an optimization with HSE06.[81,82] The auxiliary density matrix method (ADMM)[83] was employed for production as it significantly reduced the computational overhead for the hybrid functional calculations. In each case both the lattice vectors and ion positions were fully relaxed, ion positions only for the trapping calculations. The trapping energy was described as the energy of the localized charge carrier referenced to that of the free carrier (hole or electron) in the conduction or valence band. As a result all trapping energies were zero bound (no charge localization) with increasingly negative trapping energies describing more energetically favored trap states. The multiplicity of the system is allowed to relax from both the low spin (all electrons are paired) and a high spin (all undercoordinated atoms have an unpaired electron) initial guess to ensure the same solution was found and the ground state multiplicity described. The reversibility of the trapping process was determined by re-optimizing the charged geometries in the neutral charge state to ensure the original structure (and energy) was recovered and to explore those cases where trapping leads to an irreversible change to the network. To account for finite size charge effects, the Lany-Zunger[84,85] correction scheme was applied. The degree of localization was gauged from the (dimensionless) inverse participation ratio $\mathrm{IPR}(i) = \sum_j (c_{ij})^4 / (\sum_j (c_{ij})^2)^2$, where c_{ij} refers to the expansion coefficients of the i-th Kohn-Sham state in Gaussian-type orbital part of the CP2K basis set. The same concept had been used extensively to gauge the degree of localization of electronic and vibrational states in amorphous and disordered films,[59,86–90] i.e., the higher the IPR value the stronger the localization. The bandgap was then taken from the mobility edge of the valence band to the mobility edge of the conduction band, so as not to take into account the localized states that comprise the band edges.[88] Visualization and rendering were performed using the visual molecular dynamics (VMD) package.[91]

2.2. Generation of Structural Database by Advanced Statistical Sampling

An inherent challenge in the modeling of amorphous and disordered materials is defining when the model or ensemble is large enough to capture the range and frequency of structural motifs, thereby well describing configurational space. This is vital in ensuring that the presented results achieved the often-quoted statistical significance. A commonly used approach was to create an ensemble of structures that captures a range of cation and anion environments. These environments are then sampled either randomly or based on some site-centered descriptor. The challenge with this approach is constructing a structural ensemble of appropriate size.

Here, a holistic approach to the problem is demonstrated. By defining a set of structural descriptors for the system and characterizing how they are distributed, this approach allows us to verify whether the computational treatment "self-consistently converges". It also makes it possible to obtain a statistically representative subset of the ensemble, e.g., to facilitate calculations at a higher level of electronic structure theory. This is illustrated in **Figure 1** using the density as an example. Technical details and results for all other descriptors (number of undercoordinated nitrogen $N(\mathrm{N_{uc}})$, bulk modulus B, and number of four-membered atoms $N(\mathrm{FMR})$) used in this work are provided in the Supporting Information.

First, an initial ensemble of structures was produced, which provides empirical probabilities in the form of normalized histograms. This can be fitted to a normal distribution, which also yields deviations for each bin of the histogram from this analytically represented continuous reference distribution due to the finite sampling (see Figure 1a). These deviations determine the scaled mean absolute error with respect to the reference distribution $\widetilde{\mathrm{MAE}} = \Delta\rho \cdot \mathrm{MAE}$, where $\Delta\rho$ is the length of the sampling interval for the density. Adding more samples to the structural ensemble allows us to monitor the $\widetilde{\mathrm{MAE}}$ as a function of ensemble size (Figure 1b). Previous studies have used ensemble sizes given by $N_{\mathrm{samples}} < 50$,[37,39,92] a range in which $\widetilde{\mathrm{MAE}}(\rho)$ is still relatively large. From 250 to 300 samples, $\widetilde{\mathrm{MAE}}(\rho)$ decreases only insignificantly, suggesting the aforementioned "self-consistent convergence" with respect to the ensemble size. As demonstrated in the Supporting Information, for the final ensemble consisting of 300 samples at the PBE level, this also holds for the other four structural descriptors, although the convergence rate can be different from that shown in Figure 1b. While the final PBE ensemble appears to sufficiently cover the configurational space of a-Si_3N_4, the subject of this work requires calculations at the hybrid-DFT level, which are not easily tractable on a scale that large. To overcome this challenge, a statistically representative subset of the PBE ensemble is constructed by using the previously determined continuous reference distributions according to the procedure described in the Supporting Information. Figure 1c illustrates that the resulting 100 structures yield essentially the same continuous distribution for the density. Corresponding plots and results for the other five descriptors are shown in the Supporting Information.

The present approach can be easily transferred to other amorphous structures and extended to sampling at any stage – from the initial model building to identifying defect sites and beyond. It is noted that – while tempting to draw conclusions based on how a given structural property is distributed – care is needed without a clear physical driver for the reference distribution functions.

2.3. Efficient Descriptor for Local Analysis

How to appropriately describe sites within an amorphous network is inherently challenging as the convenient crystal description, where a site has defined symmetry and coordination within a regular lattice breaks down. A range of sites are present in the amorphous network, and how to characterize them conveniently is an open question. Quantifying the degree of distortion is challenging because established measures for the crystal tend to struggle: Symmetry does not work as a criterion because it is

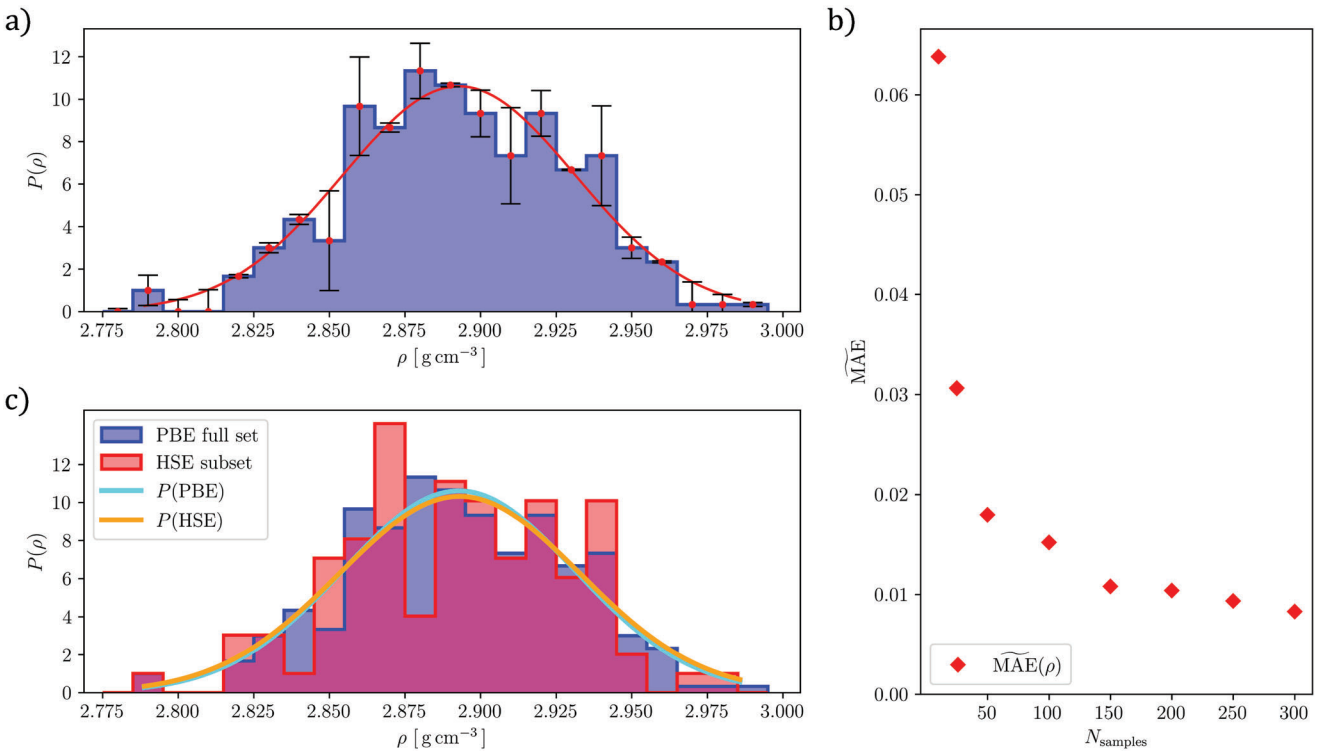

Figure 1. a) Normalized histograms for the density ρ of the final data set consisting of 300 PBE-optimized samples (blue bars). The resulting fitted continuous reference distribution function and the associated deviation for each bin are shown by red line and the error bars, respectively. The latter determine the scaled mean absolute error ($\widetilde{\text{MAE}}$) for $N_{\text{samples}} = 300$, which is shown in b) as function of ensemble size. c) Normalized histograms for the density ρ (red bars) and concomitant fitted continuous distribution function (orange line) for the reduced but statistically representative subset of the full final PBE data set, which has been used for the HSE calculations. Histograms and reference distribution for the full data set are repeated from a) and shown in the background (as blue bars and cyan line, respectively).

broken in the amorphous phase, even on a local level. Measuring bond lengths and angles comes with the problem that each coordination polyhedron employs a set of angles and pair distances. In the case of a tetrahedron, there are four bonds and six bond angles in total. Relying only on the widest angle or the most elongated bond is unsuitable for measuring distortion because it neglects the interplay with the others. Considering the complete local distribution of bonds and angles instead is impractical, as averages mask a lot of the detail for highly distorted polyhedra. Also, the local distributions suffer from the small set of values leading to noise limiting their meaningfulness.

To overcome those issues, a novel site-based descriptor has been introduced inspired by the concept of Tolman's angle commonly used in coordination chemistry.[93] The idea is to invert the original concept and construct a cone in the largest of the coordination polyhedron's faces with the tip fixed on the central atom to measure the empty space in the coordination environment (**Figure 2**a). By doing so, the cone describes the empty space

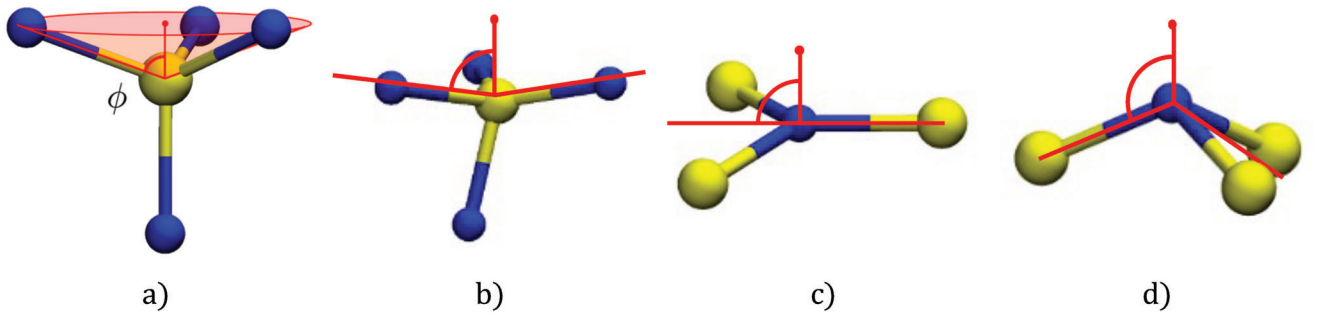

Figure 2. Illustration of the cone to quantify the distortion in polyhedra: a) A cone is constructed at a polyhedron face with the tip on the central atom. The cone axis and the bond to the nearest neighbor (slant height) span the cone angle ϕ. For an ideal tetrahedron, $\phi = 70.53°$. b,d) Illustration of a set of common (distorted) coordination environments: b) SiN_4 tetrahedron with a widened face leading to an increase of ϕ yielding $70.53° < \phi < 90°$, c) the borderline case of an ideal trigonal-planar NSi_3 configuration with $\phi = 90°$, d) an elevated NSi_3 leading to a trigonal-planar with $\phi > 90°$.

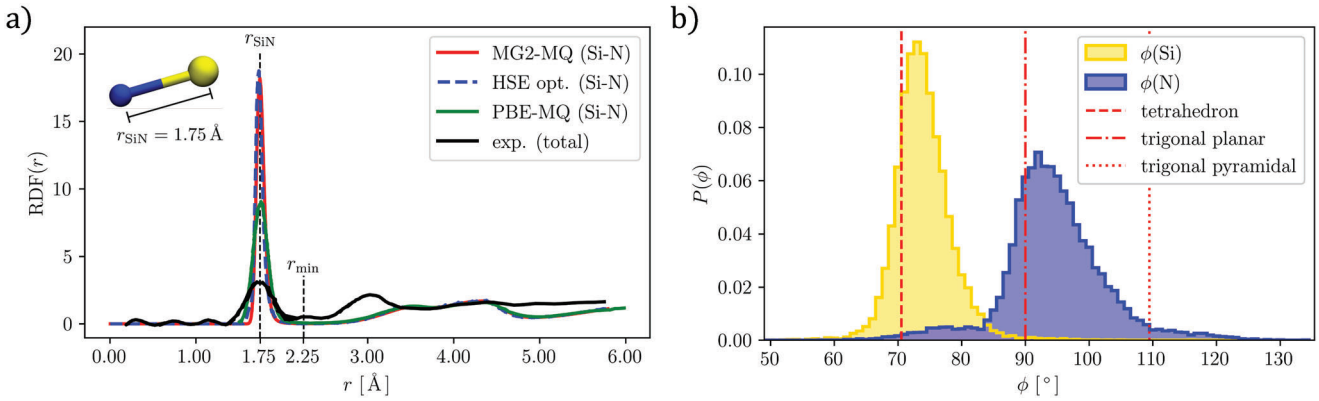

Figure 3. a) The radial distribution function (RDF) of silicon-nitrogen (Si-N) pairs plotted against the pair distance *r* of the structures generated with the MG2-FF (MG2-MQ) and the optimized structures (HSE opt.). For comparison, data from PBE-based MQ-study (PBE-MQ)[39] and x-ray diffraction experiments[28] are included. The experimental RDF cannot distinguish between elements and thus includes contributions N-N and Si-Si pairs, both of which contribute to the broad peak centered at 3.0 Å (see Supporting Information). b) Distribution *P* of the cone angle ϕ for silicon (yellow) and nitrogen (blue). Red lines indicate the cone angle of the cone angles of the ideal tetrahedron (dashed), the ideal trigonal planar (dash-dotted), and the ideal trigonal pyramidal configuration (dotted). All data is from HSE-optimized structures.

between the binding partners of an atom and, especially, captures deformation by the widening of a polyhedron face, regardless of whether it is caused by bond elongation or bond angle widening. Due to the symmetry of the cone, it captures the deformation by a single number, namely the angle at the tip, reducing the problem's complexity. Also, it can be transferred to any (amorphous) network and coordination geometry. Common coordination patterns are shown in Figure 2b,d, and an even more elaborated set of polyhedra is given in the Supporting Information. The reference values for an ideal tetrahedron, an equilateral triangle, and a trigonal pyramid are 70.53°, 90°, and 109.47°, respectively. In the following sections, ϕ will be used to characterize the coordination geometries and their (seamless) change during charge trapping processes.

2.4. Validation of Computational Model by Characterization of Basic Properties

Before the modes of charge trapping in a-Si_3N_4 can be linked to structural motifs, verifying if the models accord with the existing experimental and computational data is important. Results presented here and in the following are based on a MQ procedure with cells containing 280 atoms and a cooling rate of 1 K ps^{-1}, which has yielded structural ensembles consisting of 300 samples at the PBE level and a statistically representative subset of 100 samples at the HSE06 level. As already noted in the previous sections and further detailed in the Supporting Information, these settings have been carefully tested and consistently chosen. There is a good agreement between the approach employed here and previous experimental and theoretical studies of a-Si_3N_4 (see **Figure 3**). The average density of is $\rho = 2.9$ g cm^{-3}, which matches both experimental[16,28,29] and simulation studies.[43,68,94] Equally, the mean Si-N bond length ($r_{SiN} = 1.75$ Å), mean angles ($\theta_{NSiN} = 109°$, $\theta_{SiNSi} = 120°$), and the mean bulk modulus ($B = 166$ GPa) agree with values reported in the literature.

The RDF for Si-N pairs in Figure 3a shows a sharp peak at 1.75 Å with a standard deviation of $\sigma_{RDF}^{MG2} = 0.04$ Å. The value agrees with the Si-N bond length in the β-Si_3N_4 [95] and x-ray scattering experiments on a-Si_3N_4.[28] The shape of the curve is maintained under DFT optimization and matches the one of a fully DFT-driven MQ by Kang et al.[39] The local minimum after the first peak at $r_{min} = 2.25$ Å is used in the following as a short-range cut-off radius to define the first coordination sphere. It is important to note that this radius is considerably larger (28%) than the equilibrium bond length, and the RDF does not become zero.

Table 1. Comparison in coordination number between the calculated results and the experimentally reported values.[29]

Atom type	Experiment[29]	This work (HSE)
Si	3.70	3.96
N	2.78	2.87

Another feature of a-Si_3N_4 is the appearance of undercoordinated atoms; the effective coordination numbers for both elements are listed in **Table 1**. The silicon atoms are 0.37% undercoordinated, whereas, for nitrogen atoms, the deviations are more significant, with 4.8%. Off-coordinated atoms are a ubiquitous feature of both experimental and theoretical[38–40,43] studies. Furthermore, neutron scattering experiments by Misawa et al.[29] found dangling bonds are the most present defective species with coordination numbers of 3.7 and 2.78 for Si and N, respectively. However, statements on the concentration in all studies must be treated with care as an undefined portion of the signal originates from interfaces with substrates, which is not considered in these models.

An examination of the local structure in a-Si_3N_4 points toward considerably distorted coordination polyhedra, with a coordination sphere that is largely intact. As shown in Figure 3b, the distribution $P(\phi(Si))$ of SiN_4 tetrahedra is shifted toward larger values than the ideal tetrahedron, with an average of 74.0° ± 3.5°. Thus, most tetrahedra have at least one face flattened with respect to the undistorted tetrahedron. Analogously, $P(\phi(N))$ is shifted to larger values (average 94.3° ± 5.5°), indicating nitrogen being

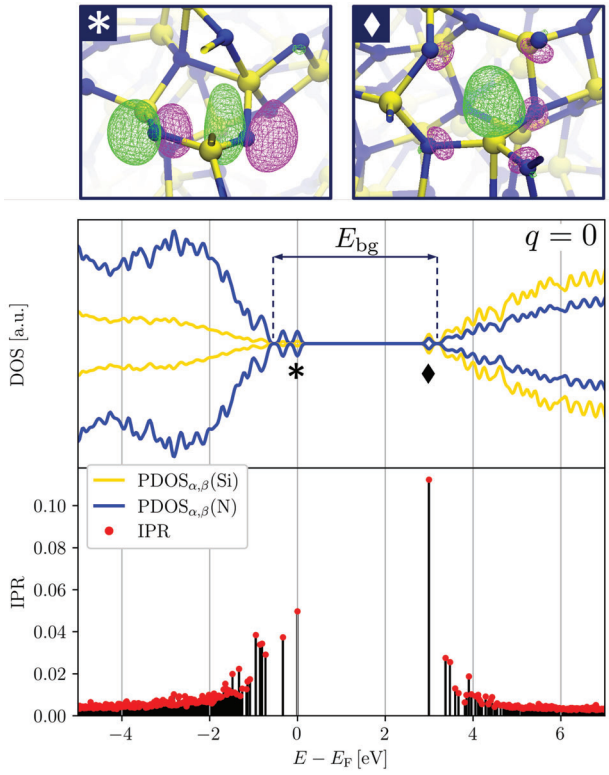

Figure 4. Upper panel: Illustration of the band edge states localized on two-coordinated nitrogen atoms above the VBM (*) and localized on distorted Si-tetrahedron below the CBM (✦). The isosurfaces of the spin density are set to 0.05 e Å^{-3}. Middle panel: The projected electronic density of states (DOS) of Si (yellow) and N (blue) in a single neutral a-Si_3N_4 configuration relative to the Fermi level E_F. The bandgap E_{bg} is measured by excluding the localized states labeled with *, ✦. Lower panel: The inverse participation ratio for all eigenstates with -5 eV < E-E_F < 7 eV. All data is obtained from a DFT calculation at the HSE06 level.

displaced out of the triangle's plane. The tails in both distributions highlight the range in coordination environments, predominantly capturing distinct sites for N and a small number of undercoordinated Si.

The examination of the electronic structure agrees with previous studies, where the valence band maximum (VBM) is predominantly N-character, and the conduction band minimum (CBM) is Si-character. A representative example of the electronic density of states (DOS) is shown in **Figure 4**. The average bandgap is 4.43 eV with localized states introduced at the band edges as confirmed in the IPR, typically assigned to the presence of coordination defects at band edges.[38–40] The localized states vary from cell to cell in number and energetic separation because the associated defective sites are not uniform in their severity of distortion. The localized states above the VBM are centered on a handful of predominantly two-coordinated N atoms. In contrast, the ones below the CBM are centered on a distorted or three-coordinated Si atom, which appears rarer but is associated with a higher degree of localization. It is possible that there is more than one single potential trap site per box available. Still, since the boxes get only singly charged, only the highest occupied and the lowest unoccupied state are of relevance here. The cells all have a low spin electronic ground state such that the dangling bonds are either unoccupied or fully occupied ($N^0 + K^0 \rightarrow N^- + K^+$), in accordance with the negative-U character of the dangling bond centers.[20]

3. Results and Discussion

3.1. Hole Trapping

As described in Section 2.4, the nature of the VBM is of predominantly N-character, with the frontier states resulting from two-coordinated N-atoms. On the removal of an electron from the system, the hole localizes over the two-coordinated N-sites making up the VBM. On geometric relaxation, the hole localizes on one or two N atoms with at least one being two-coordinated. The relaxation on hole trapping is limited with an average N-Si bond elongation of 0.2 Å and the coordination sphere of all atoms remaining unaffected. This is shown schematically in **Figure 5**a. In the uncharged state, the two-coordinated N atoms have a negative polarization compared to the three-coordinated site. The relaxed hole state moves from the vicinity of the VBM toward the midgap. The average trapping energies are generally small (0.35 eV) for the majority of configurations, as shown in Figure 5d. The trap levels sit in the bottom half of the bandgap, with most values between the VBM and 1.1 eV above the VBM. This accords well with previous experimental characterization of the shallow hole traps in a-Si_3N_4.[96–98] Two outliers show pronounced trapping energies with trapping energies as high as −1.83 eV and result in significant relaxation.

Closer examination of the trapping sites reveals two distinct types; in most cases, the hole is localized on a single N (Figure 5a) with a small polarization on the neighboring N. For 10% of sites, the hole is shared between two adjacent two-coordinated N (Figure 5b). The frequency of the two-center trap is limited by the scarcity of two-coordinated N and the prerequisite that two are present at adjacent sites (sharing a single Si center). The local environment dictates how the hole is shared between the center (Figure 5c), where both centers are free to relax the hole is evenly shared between N ($\mu_s \rightarrow 0.5$). Where the relaxation of the N center is frustrated the hole increasingly sits on a single N ($\mu_s \rightarrow 1.0$). There is no meaningful correlation in the trapping energy as a function of type, as the majority of the trapping energies sit in a narrow range, with the energy range dictated by the local environment.

These sites are analogous to the previously characterized N-centers, where the trapping energies and relaxation accord well with previous work, updated here with an improved description of the electronic structure and extensive sampling of the sites available in a-Si_3N_4.[21–26]

3.2. Electron Trapping

3.2.1. Trapping at Three-Coordinated Si (K-Center)

Structurally the K-centers are similar to those previously described by Kang et al.[39] and others[97,99] in substoichiometric a-Si_3N_4. It is important to note that for stoichiometric a-Si_3N_4 in

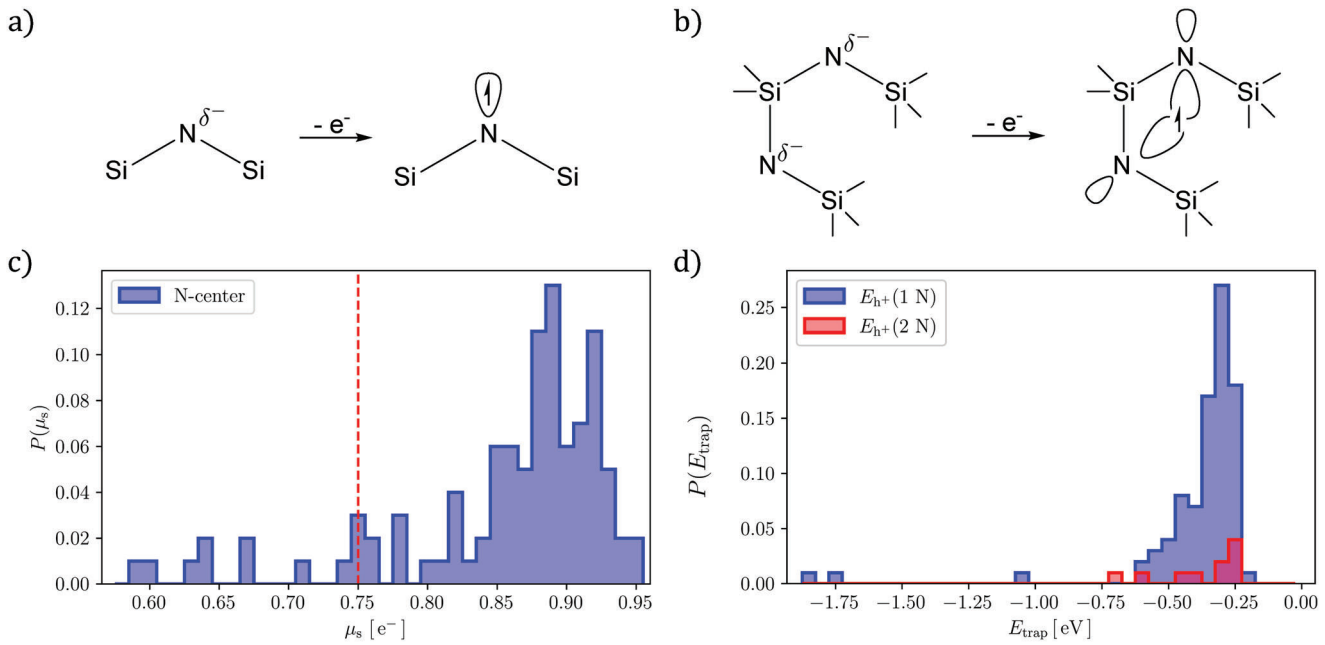

Figure 5. a) Schematic illustration of hole polaron formation by removing an electron on two-coordinated N-atom and b) on a pair of two-coordinated N-atoms. c) Distribution of spin momenta μ_s of the corresponding singly-occupied electronic state localized on N-atom trapping sites. $\mu_s < 0.75e^-$ (red dashed line) are considered localized over two atoms. d) Distribution of hole trapping energies E_{h+} for the localized and the shared traps (1 N, 2 N).

all cases, the ground state configuration for the three-coordinated Si is positively charged and low spin (nominally K^+ as schematically depicted in **Figure 6**a. This pathway of charge trapping occurs in 31 of 100 hundred boxes within the ensemble of models. Characterization using the Tolman-inspired cone angles ϕ_K (see Section 2.3) yields the distribution shown in Figure 6b (for $\phi_K(q = 0)$), which reveals that the K-centers range from planar trigonal to the trigonal pyramidal coordination, peaked at the former, but with most structures sitting in an intermediate geometry. On trapping an electron, the peak of this distribution changes from 92.7° to 106.7° (see $P(\phi_K(q = -1))$ in Figure 6b, i.e., the structure relaxes to toward trigonal pyramidal geometry. The unpaired electron occupies the vacant tetrahedral bonding site. This site emerges after the structural relaxation of the Si out of the N-N-N plane, the amount of which is quantified via d_{oop} as sketched in Figure 6a. The magnitude of the relaxation is typically small such that the relative distances in the first coordination shell are hardly affected. In all cases, the electron is localized on a single Si-atom leaking out slightly toward the neighboring atoms. There is a strong correlation between the position of the empty Si-state in the bandgap and the geometry. In the trigonal planar configuration, the empty Si-state is degenerate with the CBM, whereas the trigonal pyramidal configurations give rise to mid-gap states. As a result, the majority fall between the extreme cases giving rise to states in the upper half of the bandgap.

As shown in Figure 6c (green bars), the trapping energies are typically small with an average of −0.55 eV and the majority clustered around the mean. However, several sites show trapping energies with significantly larger absolute values as a result of the local environment. Investigating the link between the trapping energy and the magnitude of the displacement due to relaxation Δd_{oop} yields two trends visualized in Figure 6c,d: There are some traps clustered around −0.5 eV without a meaningful link between trapping energy and displacement, with a range of displacements resulting in a narrow range of trapping energies (E_{e^-}). In contrast, there appears to be a linear trend ($\Delta E^{fit}_{e^-}/\Delta d_{oop} = -1.71 \pm 0.19$ eV Å^{-1}) where the displacement and trapping energies are strongly correlated covering an energy range from −0.27 to −1.27 eV ($E^*_{e^-}$) and displacements up to 0.55 Å. In both cases, the low trapping energies paired with the minor change in geometry lead to the electron being reversibly trapped.

3.2.2. Intrinsic Electron Trapping

The trapping considered up to this point has resulted from (under)coordination "defects" in the amorphous network providing the states that give rise to the trapping behavior. By the convention adopted in this work, electron trapping on fully coordinated atoms is considered as intrinsic trapping, which is schematically depicted in **Figure 7**a. This type of trapping occurs on (initially) fully coordinated Si atoms that deviate from the ideal tetrahedral symmetry (see Figure 7b, upper panel), analogous to intrinsic trapping in a-SiO_2 described in previous work.[57] Geometric relaxation relaxation is dominated by two nearest-neighbor N-atoms moving away from each other by an average distance of $\Delta r_{intr} = 0.2$ Å. Consequently, one face of the corresponding SiN_4 tetrahedron is distorted toward a pseudo trigonal bipyramid geometry whose equatorial position is occupied by the electron with local C_{2v} symmetry, which is schematically depicted by the "intr" configuration in Figure 7a. The average cone angle ϕ_{intr} widens from 81° to 91° (see Figure 7b, lower panel, blue histogram). For 35% (24 out of 69 simulation cells) of the intrinsic

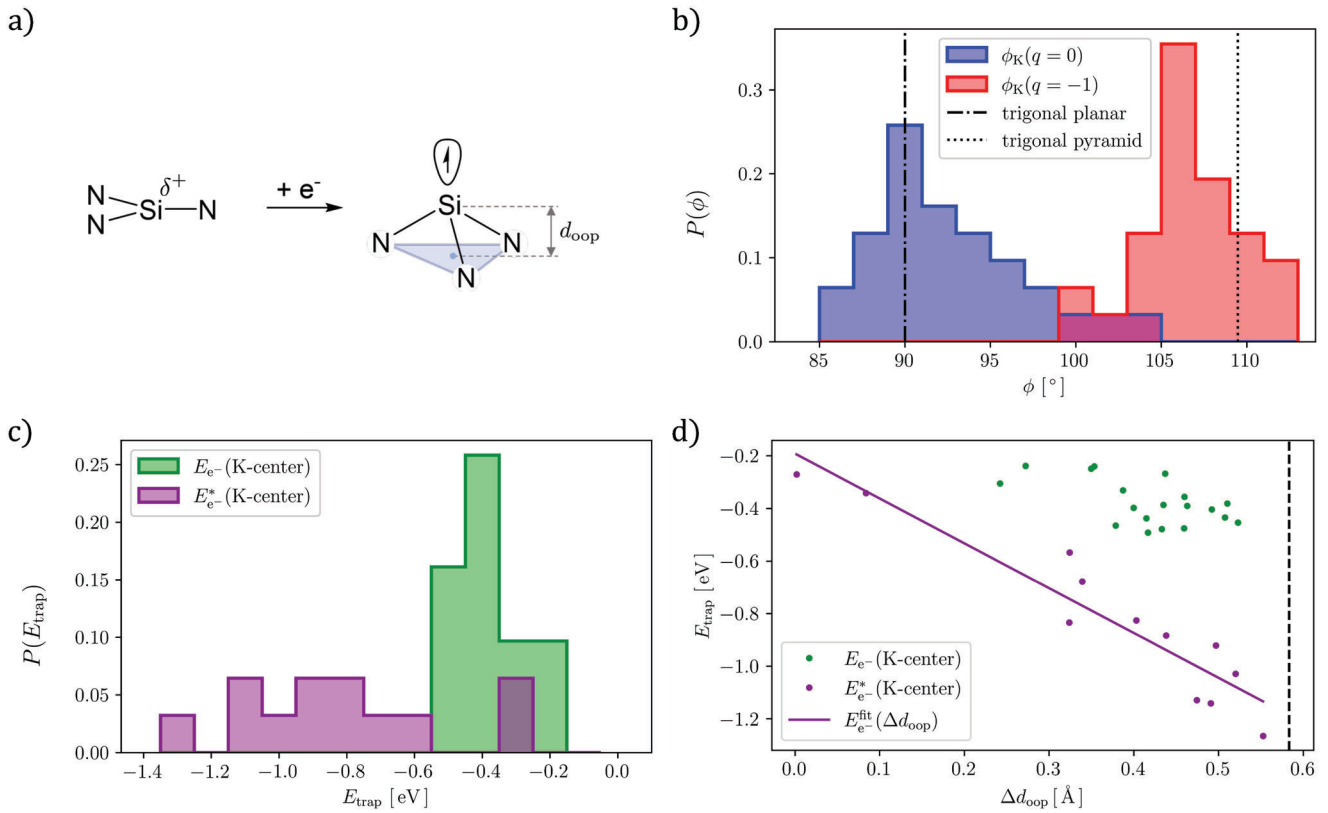

Figure 6. a) Schematic view of electron trapping at an undercoordinated Si-atom with d_{oop} being the distance of the silicon atom to the N-N-N plane. b) Distribution of cone angles ϕ_K of the trapping sites in the neutral ($q = 0$) and the charged ($q = -1$) state, with cone angles of the undistorted trigonal planar (dash-dotted line) and the trigonal pyramid (dotted line) as reference. c) Distribution of trapping energies for electrons trapped on K-centers E_{trap} and d) their correlation with the change of the trigonal pyramid's height d_{oop} (see a) during the trapping process. The black dashed line marks d_{oop} in an ideal, undisturbed SiN_4 tetrahedron. The purple circles represent the data points considered for fitting the line $E^{fit}_{e^-}(\Delta d_{oop})$ and defines the group $E^*_{e^-}$, and the remainder is labeled E_{e^-} (also in panel c).

traps the relaxation stops at this point, which makes them almost iso-structural to the intrinsic electron traps described in a-SiO_2.[57] As shown in Figure 7c (by the blue histogram), none of these intrinsic traps have trapping energies less than −1.0 eV, with a distribution closely centered around its mean of −0.6 eV and only a slight skew toward smaller energies. These states show reasonable agreement with the shallow electron trap states close to the CBM of a-Si_3N_4.[31,100,101]

a-Si_3N_4 lacks the structural flexibility inherent to a-SiO_2 because the N anions in the former are predominantly three-coordinated, leading to substantially frustrated geometric relaxation. In 56% (39 out of 69 simulation cells) the relaxation of intrinsic traps continues with one of the Si-N bonds elongating significantly, resulting in the formation of a two-coordinated N (formally N^-) and the unpaired electron on a three-coordinated Si ("iK" configuration in Figure 7a). This is iso-structural with the K-center described above as it employs the same number of neighbors. The corresponding distribution of ϕ_{iK} is centered at 106°, indicating the formation of a trigonal pyramid (see Figure 7b, lower panel, red histogram). For this reason, this subgroup of traps is referred to as induced K-centers (iK). Compared to the trapping described in Section 3.2.1 they show two important differences: First, the presence of neighboring two-coordinated N atoms, and second, there are no dangling bond states in the bandgap prior to trapping. Both facts combined allow the vast majority of these traps to be de-trapped reversibly despite trapping energies with significantly higher absolute values and an average of −1.0 eV (see Figure 7c, red histogram). This does not hold for the outliers with trapping energies even below −1.5 eV. Trapping at these outlier sites results in a pronounced distortion of the amorphous network, driven by the trapping in a strained local structure. The relaxation results in the ring opening, thereby releasing strain in a given region and irreversibly altering of the amorhphous network resulting in a K-center and a two-coordinated N atoms. The third subgroup of electron trapping geometries is identified as $N_3Si\text{-}SiN_{x\in\{3,4\}}$ motif, which occurs only in only 9% (6 out of 69 simulation cells) and is thus the rarest one. As such, care should be taken in inferring any general behavior or trends from the ensuing characterization, as a larger structural ensemble is likely required. In this case, trapping occurs on a Si-Si bond with the trapped electron shared between two Si-atoms, analogous to the N-center described for the hole trap. It is equally present in those cells that contain Si-dangling bonds and those that do not. In common with previous studies, the Si-Si trap level sits close or slightly below the CBM, although due to the limited occurrence of the $N_3Si\text{-}SiN_{x\in\{3,4\}}$ in the stoichiometric models presented here. The trapping energies sit between the intrinsic electron trap and the trap-induced K-center, with an

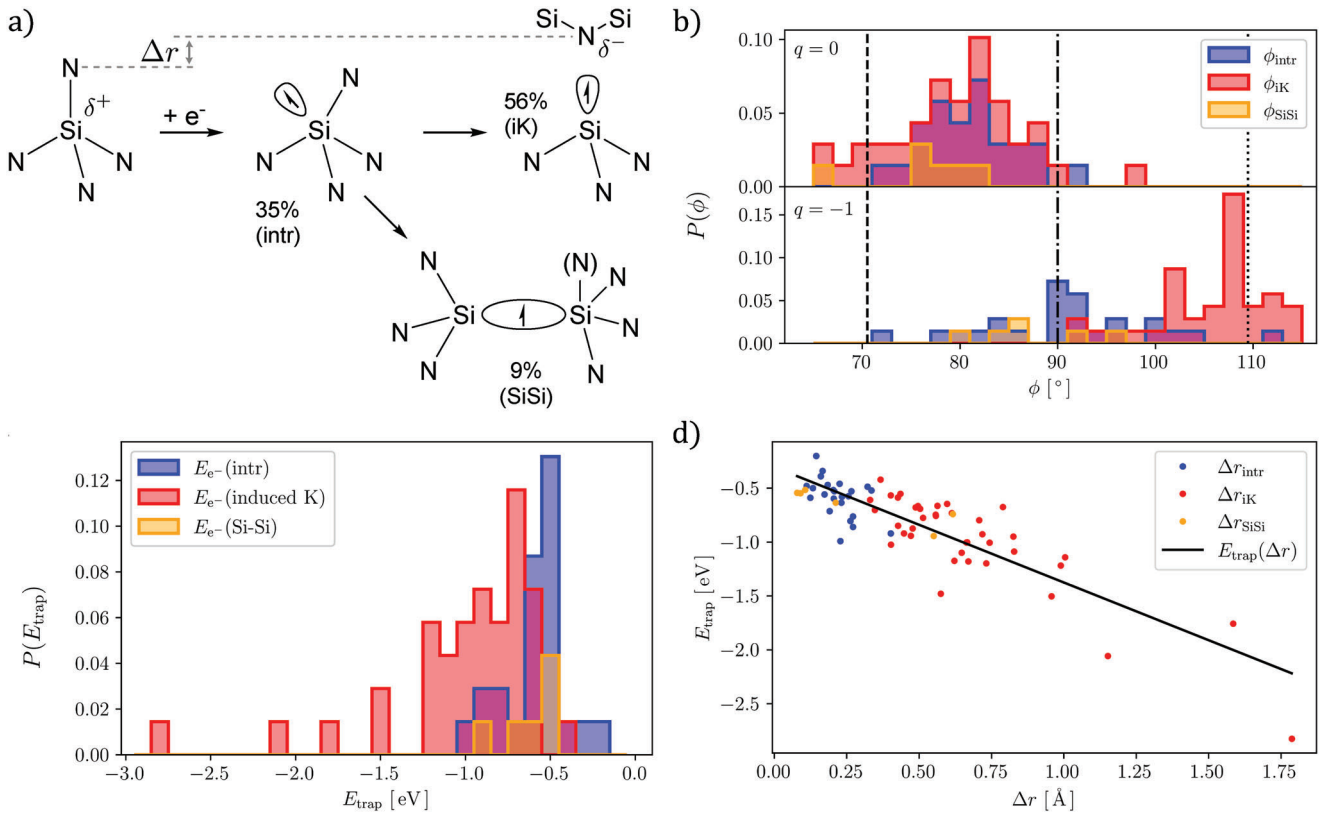

Figure 7. a) Schematic view of intrinsic electron trapping at a SiN_4 tetrahedron cut out of a-Si_3N_4, which results in intrinsic traps (intr in blue), induced K-centers (iK in red), and N_3Si-Si$N_{x\in\{3,4\}}$ dumb-bell configurations (SiSi in yellow). b) Distribution of cone angles ϕ of the trap sites of these three types of trapping configurations in the neutral ($q = 0$) and charged state ($q = -1$). The cone angles of the undistorted tetrahedron (dashed line), of the trigonal plane (dash-dotted line), and of the trigonal pyramid (dotted line) are given as references. c) Distribution of the trapping energies E_{trap} associated with the three types of trapping configurations. d) Correlation between E_{trap} and the change of nearest Si-N neighbor distances Δr due to geometric relaxation as schematically indicated in a).

average trapping energy of −0.7 eV (see Figure 7c) and a wide range of Si-Si bond lengths between 2.34 to 2.62Å.

All three trap types have in common that their trapping energy E_{trap} scale with the displacement of their nearest neighbor N atoms upon relaxation. This is illustrated in Figure 7d, where E_{trap} is plotted as a function of the largest displacement Δr in the first coordination shell of the trap site. The linear fit to the data yields a slope of −1.1 eV Å^{-1} with a standard deviation of 0.1 eV Å^{-1}.

3.3. Discussion

As might have been reasonably expected from the complex and nuanced view of charge trapping in a-Si_3N_4 presented in the literature prior to this study the picture of hole and electron trapping that is revealed is multifaceted. Hole trapping in the absence of either substoichiometry or introduced defects is found to be dominated by the two-coordinated N atoms (N-centers). The description of the N-center accords with previous studies, with trap levels close to (+0.5 eV) the VBM and low trapping energies resulting in the transient nature of the trap state. The models presented here show a substantially higher N-coordination number than the experimentally characterized films.[28,29] It is therefore reasonable to conclude that undercoordinated N plays an important role in hole trapping.

Electron trapping initially shows two distinct modes, those traps that are K-center-like, trapping on three-coordinated Si-atoms pre-existing in the network and those that are intrinsic with the trapping on fully coordinated albeit distorted Si-centers. The trapping at K-centers and N_3Si-Si$N_{x\in\{3,4\}}$ accords with the previous work for both the crystal[46,50,51] and the amorphous.[38–40] The K-center trapping levels cover a broad range of values, 0.2 to 2.0 eV, below the CBM. The trapping energies are typically small with $E_{e^-}(K) = -0.5$ eV, with a range of −0.27 to −1.25 eV. Finally, from the relationship between trapping energy and geometric relaxation two regimes are suggested. The first, where the trapping energy and the relaxation are decoupled, and the second, where the two are strongly correlated.

The intrinsic electron traps are polaronic in nature and driven by a partial localization of the CBM as a result of distorted SiN_4 motifs. The trap levels show some overlap with the K-centers described in the previous paragraph, although sit in a much tighter range, close to the CBM. On the trapping of an electron the electron is fully localized on a fully coordinated Si, there is a relaxation that results in two bonds elongating and an opening of one face of the corresponding SiN_4 tetrahedron. Until this point the relaxation is analogous to that described for intrinsic electron

polarons in SiO_2.[56,57,62] The relaxation is limited compared to a-SiO_2 as the increased nodal connectivity of the anion increases cross-linking and reduces flexibility in the network. As a result the trapping energies are lower, ≈ 50% of those of a-SiO_2, at an average $E_{e^-} = -0.6$ eV, with a range of −0.2 to −1.0 eV. The traps are reversible with respect to discharge and result in a recovery of the original geometry and energy.

All of the intrinsic electron traps initially relax as described in the previous paragraph, for 65% of the intrinsic traps the relaxation continues giving rise to either the trap-induced K-center (56%) or a trap-induced N_3Si-Si$N_{x\in\{3,4\}}$ (9%). For the trap-induced K-center, the trapping energies are more pronounced with an average E_{e^-}(iK) = −1.0 eV, with a range −0.5 to −2.8 eV. For all but the highest trapping energies, the trapping is reversible. The configurations with the highest trapping energies induce significant changes to the lattice, thereby allowing strained motifs to relax. The magnitude of the relaxation (>1Å) makes recovery of the original structure impossible. A similar picture emerges for the trap-induced N_3Si-Si$N_{x\in\{3,4\}}$, the initial relaxation elongates a Si-N bond, and for the trap-induced K-center the relaxation is dominated by the N moving away. In the induced N_3Si-Si$N_{x\in\{3,4\}}$ the local environment both the N and Si relax resulting in the back projection of Si through the N-plane where it interacts with an adjacent distorted SiN_4 that undergoes relaxation to form N_3Si-Si$N_{x\in\{3,4\}}$. For the defects described here, the process is reversible although as previously noted the limited sampling of the induced N_3Si-Si$N_{x\in\{3,4\}}$ makes definitive statements impossible.

There are a number of points of note, there is no analogous single electron process seen in the intrinsic trapping behavior of a-SiO_2 – which we consider as reference system here. Forming an electron bi-polaron has been shown to result in oxygen atom being pushed into an interstitial where the excess charge is being localized (O_i^{2-}), leaving a neutral oxygen vacancy (V_O^0) behind. This process either happens spontaneously or via a small barrier. The frustrated relaxation in a-Si_3N_4 favors the elongation of a Si-N bond, the same lack of flexibility ensures the reversibility of the process, trapping the two-coordinated N in the vicinity of the three-coordinated Si. Resulting in a modification to the amorphous network both reversibly and irreversibly upon the trapping of a single electron requires careful consideration. In a-SiO_2 a single electron is trapped reversibly at wide O-Si-O bond angles, whereas the electron bi-polaron results in an irreversible modification to the lattice as noted. For a-Si_3N_4 an intermediate behavior is found, the electron trapping begins being analogous to a-SiO_2 showing similar initial trapping geometries and relaxations, albeit frustrated as a result of increased anion connectivity. The lack of structural flexibility drives the structural modifications that result in trap-induced K-centers and N_3Si-Si$N_{x\in\{3,4\}}$. What is both interesting and perhaps unexpected is that both of the active defects in charge trapping memory are reversibly generated as a result of intrinsic electron trapping.

The trap-induced formation of K-centers has important implications for the understanding of defect concentration and how it may evolve over a series of charge/discharge cycles, i.e., read/write cycles in memory device applications. It also makes the K-center concentration something of a moving target, as some K-centers will be invisible prior to charging and upon charging the defect levels sit in an identical range to the native K-centers. Lateral leakage in this context will be mediated by the trap concentration and distribution in the material, and as such intrinsic traps, induced and native K-centers would play a role. From an application perspective, the presence of the trap-induced K-center – while not the target trapping center – has the same characteristics as the native K-center. So it would not be expected to be detrimental to performance, aside from the potential role in lateral leakage previously referenced and dictated by concentration.[99,102,103] For a-Si_3N_4 in gate dielectric applications, the implications are potentially more serious, the propensity for intrinsic trapping and the generation of trap-induced K-centers would provide a vector for the charging of the dielectric layer. The implication being that the threshold voltage instability and time-dependent dielectric breakdown are driven via intrinsic trapping and as such difficult to avoid. Finally, in the case of a-Si_3N_4 ReRAM this sheds light on the process of electro-forming and switching in a-Si_3N_4, with intrinsic trapping as the first step, followed by structural relaxation to generate the conductive filament. The high resistance state is then recovered via the reverse process, hole-trapping followed by structural relaxation to recover the original structure.

4. Conclusion and Summary

In summary, the nuanced modes of hole and electron trapping within stoichiometric a-Si_3N_4 have been investigated by combining atomistic calculations at the force field and DFT level with both PBE and HSE06. By introducing a statistical sampling method to quantify the statistical completeness of structural models obtained from a melt-quench procedure, in combination with a powerful local descriptor inspired by Tolman's angle, both structural and energetic properties of the variety of sites within the amorphous network have been systematically characterized and correlated. Hole trapping is found to be via two-coordinated N, which make up the VBM. The trapping energies are in general low and there is little perturbation to the lattice in agreement with previous observations. This suggests that in stoichiometric a-Si_3N_4 two-coordinated N dominate the shallow hole traps. The electron trapping shows two initial trapping modes either via K-centers, where the electron localizes on a single three-coordinated Si, alternatively, trapping occurs on a fully coordinated Si forming an intrinsic electron polaron. For 35% of the intrinsic trap sites the relaxation stops at this stage. However, the majority (65%) of the intrinsic electron traps relax further forming either a trap-induced K-center (56%) or N_3Si-Si$N_{x\in\{3,4\}}$ (9%). These result in a reversible modification to the amorphous network that leads to analogs of the much-discussed defects in charge trapping memory. This intrinsic trap-induced defect formation requires a revision to our understanding of trap states in a-Si_3N_4, as the concentration measured is intrinsically linked to the observation conditions. Finally, this provides important insights to the mechanism of leakage in a-Si_3N_4 films and electro-forming in a-Si_3N_4 ReRAM.

Supporting Information

Supporting Information is available from the Wiley Online Library or from the author.

Acknowledgements

This research was co-financed by Holland High Tech through a public–private partnership in research and development within the Dutch top sector of High-Tech Systems and Materials (HTSM). This work used the Dutch national e-infrastructure with the support of the SURF Cooperative using grant no. EINF-3219 and EINF-4531.

Conflict of Interest

The authors declare no conflict of interest.

Data Availability Statement

The data that support the findings of this study are openly available in Zenodo at https://doi.org/10.5281/zenodo.8239086.

Keywords

amorphous Si_3N_4, defects, DFT-HSE06 calculations, intrinsic charge trapping, statistical sampling

Received: October 6, 2023
Published online:

[1] J. S. Meena, S. M. Sze, U. Chand, T.-Y. Tseng, *Nanoscale Res. Lett.* **2014**, *9*, 1.
[2] V. Y. Doo, D. R. Nichols, G. A. Silvey, *J. Electrochem. Soc.* **1966**, *113*, 1279.
[3] A. Okada, *J. Eur. Ceram. Soc.* **2008**, *28*, 1097.
[4] F. L. Riley, *J. Am. Ceram. Soc.* **2000**, *83*, 245.
[5] S. Lina, A. Chin, F. Yeh, S. McAlister, in *2008 IEEE International Electron Devices Meeting*, IEEE, New York **2008**, pp. 1–4.
[6] A. Shaposhnikov, I. Petrov, V. Gritsenko, C. Kim, *Phys. Solid State* **2007**, *49*, 1628.
[7] A. Arreghini, F. Driussi, E. Vianello, D. Esseni, M. J. van Duuren, D. S. Golubovic, N. Akil, R. van Schaijk, *IEEE Trans. Electron Devices* **2008**, *55*, 1211.
[8] C.-Y. Lu, *J. Nanosci. Nanotechnol.* **2012**, *12*, 7604.
[9] L. Wang, C.-H. Yang, J. Wen, *Electron. Mater. Lett.* **2015**, *11*, 505.
[10] A. A. Gismatulin, G. N. Kamaev, V. N. Kruchinin, V. A. Gritsenko, O. M. Orlov, A. Chin, *Sci. Rep.* **2021**, *11*, 2417.
[11] Y. Chen, *IEEE Trans. Electron Devices* **2020**, *67*, 1420.
[12] M. Herrmann, A. Schenk, *J. Appl. Phys.* **1995**, *77*, 4522.
[13] Y. Fujisaki, *Jpn. J. Appl. Phys.* **2013**, *52*, 040001.
[14] A. Padovani, L. Larcher, D. Heh, G. Bersuker, V. Della Marca, P. Pavan, *Appl. Phys. Lett.* **2010**, *96*, 223505.
[15] S. Hu, D. Kerr, L. Gregor, *Appl. Phys. Lett.* **1967**, *10*, 97.
[16] T. L. Chu, J. Szedon, C. Lee, *Solid-State Electron.* **1967**, *10*, 897.
[17] J. Robertson, M. J. Powell, *Appl. Phys. Lett.* **1984**, *44*, 415.
[18] J. Robertson, *Philos. Mag., B* **1991**, *63*, 47.
[19] J. Robertson, *MRS Online Proceedings Library (OPL)* **1992**, *284*, 65.
[20] J. Robertson, W. Warren, J. Kanicki, *J. Non-Cryst. Solids* **1995**, *187*, 297.
[21] W. L. Warren, P. M. Lenahan, S. E. Curry, *Phys. Rev. Lett.* **1990**, *65*, 207.
[22] D. T. Krick, P. M. Lenahan, J. Kanicki, *Phys. Rev. B* **1988**, *38*, 8226.
[23] W. L. Warren, P. M. Lenahan, *Phys. Rev. B* **1990**, *42*, 1773.
[24] W. Warren, J. Kanicki, F. Rong, E. Poindexter, *J. Electrochem. Soc.* **1992**, *139*, 880.
[25] W. Warren, J. Robertson, J. Kanicki, *Appl. Phys. Lett.* **1993**, *63*, 2685.
[26] W. L. Warren, J. Kanicki, E. H. Poindexter, *Colloids Surf. A Physicochem. Eng. Asp.* **1996**, *115*, 311.
[27] P. Lenahan, D. Krick, J. Kanicki, *Appl. Surf. Sci.* **1989**, *39*, 392.
[28] T. Aiyama, T. Fukunaga, K. Niihara, T. Hirai, K. Suzuki, *J. Non-Cryst. Solids* **1979**, *33*, 131.
[29] M. Misawa, T. Fukunaga, K. Niihara, T. Hirai, K. Suzuki, *J. Non-Cryst. Solids* **1979**, *34*, 313.
[30] K. W. K. Wakita, H. H. H. Hayashi, Y. N. Y. Nakayama, *Jpn. J. Appl. Phys.* **1996**, *35*, 5R 2557.
[31] S.-J. Tsai, C.-L. Wang, H.-C. Lee, C.-Y. Lin, J.-W. Chen, H.-W. Shiu, L.-Y. Chang, H.-T. Hsueh, H.-Y. Chen, J.-Y. Tsai, Y.-H. Lu, T.-C. Chang, L.-W. Tu, H. Teng, Y.-C. Chen, C.-H. Chen, C.-L. Wu, *Sci. Rep.* **2016**, *6*, 28326.
[32] S. V. Deshpande, E. Gulari, S. W. Brown, S. C. Rand, *J. Appl. Phys.* **1995**, *77*, 6534.
[33] B. S. Sahu, F. Delachat, A. Slaoui, M. Carrada, G. Ferblantier, D. Muller, *Nanoscale Res. Lett.* **2011**, *6*, 1.
[34] S. Mohammed, M. T. Nimmo, A. V. Malko, C. L. Hinkle, *J. Vac. Sci. Technol. A* **2014**, *32*, 021507.
[35] S.-Y. Ren, W. Ching, *Phys. Rev. B* **1981**, *23*, 5454.
[36] C.-L. Wu, W.-S. Chen, Y.-H. Su, *Surf.Sci.* **2012**, *606*, L51.
[37] L. Hintzsche, C. Fang, T. Watts, M. Marsman, G. Jordan, M. Lamers, A. Weeber, G. Kresse, *Phys. Rev. B* **2012**, *86*, 235204.
[38] L. E. Hintzsche, C. M. Fang, M. Marsman, G. Jordan, M. W. P. E. Lamers, A. W. Weeber, G. Kresse, *Phys. Rev. B* **2013**, *88*, 155204.
[39] G. Kang, D. Lee, K. Lee, J. Kim, S. Han, *Phys. Rev. Appl.* **2018**, *10*, 064052.
[40] C. Wilhelmer, D. Waldhoer, L. Cvitkovich, D. Milardovich, M. Waltl, T. Grasser, *Nanomaterials* **2023**, *13*, 2286.
[41] C. M. Marian, M. Gastreich, J. D. Gale, *Phys. Rev. B* **2000**, *62*, 3117.
[42] E. Adabifiroozjaei, S. S. Mofarah, H. Ma, Y. Jiang, M. H. N. Assadi, T. S. Suzuki, *Comput. Mater. Sci.* **2020**, *178*, 109632.
[43] A. Dasmahapatra, P. Kroll, *Comput. Mater. Sci.* **2018**, *148*, 165.
[44] X. Chen, Y.-W. Wang, X. Liu, X.-B. Wang, Y.-Q. Zhao, *J. Non-Cryst. Solids* **2015**, *414*, 1.
[45] G. Pacchioni, D. Erbetta, *Phys. Rev. B* **2000**, *61*, 15005.
[46] C. Di Valentin, G. Palma, G. Pacchioni, *J. Phys. Chem. C* **2011**, *115*, 561.
[47] E. Vianello, L. Perniola, P. Blaise, G. Molas, J. P. Colonna, F. Driussi, P. Palestri, D. Esseni, L. Selmi, N. Rochat, C. Licitra, D. Lafond, R. Kies, G. Reimbold, B. de Salvo, F. Boulanger, in *2009 IEEE International Electron Devices Meeting (IEDM)*, IEEE, Baltimore **2009**, pp. 1–4.
[48] D. Milardovich, C. Wilhelmer, D. Waldhoer, L. Cvitkovich, G. Sivaraman, T. Grasser, *J. Chem. Phys.* **2023**, *158*, 19.
[49] R. Degraeve, M. Cho, B. Govoreanu, B. Kaczer, M. B. Zahid, G. van den Bosch, J. van Houdt, M. Jurczak, G. Groeseneken, in *2009 International Conference on Solid State Devices and Materials*, The Japan Society of Applied Physics, Sendai, **2009**, pp. 150–151.
[50] V. Gritsenko, T. Perevalov, O. Orlov, G. Y. Krasnikov, *Appl. Phys. Lett.* **2016**, *109*, 062904.
[51] V. Gritsenko, V. Kruchinin, I. Prosvirin, Y. N. Novikov, A. Chin, V. Volodin, *J. Exp. Theor. Phys.* **2019**, *129*, 924.
[52] V. Gritsenko, Y. N. Novikov, A. Shaposhnikov, Y. N. Morokov, *Semiconductors* **2001**, *35*, 997.
[53] M. Petersen, Y. Roizin, *Appl. Phys. Lett.* **2006**, *89*, 053511.
[54] D. Mora-Fonz, A. L. Shluger, *Adv. Electron. Mater.* **2020**, *6*, 1900760.
[55] G. Bersuker, J. Sim, C. Park, C. Young, S. Nadkarni, R. Choi, B. Lee, in *2006 IEEE International Reliability Physics Symposium Proceedings*, IEEE, New York **2006**, pp. 179–183.
[56] J. W. Strand, J. Cottom, L. Larcher, A. L. Shluger, *Phys. Rev. B* **2020**, *102*, 014106.
[57] A.-M. El-Sayed, M. B. Watkins, V. V. Afanas' ev, A. L. Shluger, *Phys. Rev. B* **2014**, *89*, 125201.

[58] D. Waldhoer, C. Schleich, A.-M. El-Sayed, T. Grasser, in *Oxide-based Materials and Devices XIV*, (Eds.: D. J. Rogers, F. H. Teherani), vol. *12422*, International Society for Optics and Photonics, SPIE, Bellingham, WA **2023**, p. 1242203.
[59] J. Strand, P. La Torraca, A. Padovani, L. Larcher, A. L. Shluger, *J. Appl. Phys.* **2022**, *131*, 234501.
[60] K. Konstantinou, F. C. Mocanu, T.-H. Lee, S. R. Elliott, *Nat. Commun.* **2019**, *10*, 3065.
[61] K. Konstantinou, S. R. Elliott, *Phys. Status Solidi Rapid Res. Lett.* **2023**, *17*, 2200496.
[62] D. Z. Gao, J. Strand, M. S. Munde, A. L. Shluger, *Front. Phys.* **2019**, *7*, 43.
[63] P. W. Anderson, *Phys. Rev.* **1958**, *109*, 1492.
[64] S. B. Bibyk, V. J. Kapoor, *J. Appl. Phys.* **1981**, *52*, 7313.
[65] Y. Park, W. Jackson, N. Johnson, S. Hagstrom, *J. Appl. Phys.* **1990**, *68*, 5212.
[66] A. P. Thompson, H. M. Aktulga, R. Berger, D. S. Bolintineanu, W. M. Brown, P. S. Crozier, P. J. in 't Veld, A. Kohlmeyer, S. G. Moore, T. D. Nguyen, R. Shan, M. J. Stevens, J. Tranchida, C. Trott, S. J. Plimpton, *Comput. Phys. Commun.* **2022**, *271*, 108171.
[67] V. V. Le, T. H. Dinh, *J. Non-Cryst. Solids* **2022**, *581*, 121381.
[68] P. Kroll, *J. Non-Cryst. Solids* **2001**, *293-295*, 238.
[69] S. Nosé, *J. Chem. Phys.* **1984**, *81*, 511.
[70] S. Nosé, *Mol. Phys.* **1984**, *52*, 255.
[71] W. G. Hoover, *Phys. Rev. A* **1985**, *31*, 1695.
[72] S. Le Roux, P. Jund, *Comput. Mater. Sci.* **2010**, *49*, 70.
[73] K. Goetzke, H.-J. Klein, *J. Non-Cryst. Solids* **1991**, *127*, 215.
[74] X. Yuan, A. N. Cormack, *Comput. Mater. Sci.* **2002**, *24*, 343.
[75] T. D. Kühne, M. Iannuzzi, M. Del Ben, V. V. Rybkin, P. Seewald, F. Stein, T. Laino, R. Z. Khaliullin, O. Schütt, F. Schiffmann, D. Golze, J. Wilhelm, S. Chulkov, M. H. Bani-Hashemian, V. Weber, U. Borštnik, M. Taillefumier, A. S. Jakobovits, A. Lazzaro, H. Pabst, T. Müller, R. Schade, M. Guidon, S. Andermatt, N. Holmberg, G. K. Schenter, A. Hehn, A. Bussy, F. Belleflamme, G. Tabacchi, et al.*J. Chem. Phys.* **2020**, *152*, 194103.
[76] J. VandeVondele, J. Hutter, *J. Chem. Phys.* **2007**, *127*, 114105.
[77] Goedecker, Teter, Hutter, *Phys. Rev. B* **1996**, *54*, 1703.
[78] C. Hartwigsen, S. Goedecker, J. Hutter, *Phys. Rev. B* **1998**, *58*, 3641.
[79] J. P. Perdew, K. Burke, M. Ernzerhof, *Phys. Rev. Lett.* **1996**, *77*, 3865.
[80] J. P. Perdew, K. Burke, M. Ernzerhof, *Phys. Rev. Lett.* **1997**, *78*, 1396.
[81] J. Heyd, G. E. Scuseria, M. Ernzerhof, *J. Chem. Phys.* **2003**, *118*, 8207.
[82] J. Heyd, G. E. Scuseria, M. Ernzerhof, *J. Chem. Phys.* **2006**, *124*, 219906.
[83] M. Guidon, J. Hutter, J. VandeVondele, *J. Chem. Theor. and Comp.* **2010**, *6*, 2348.
[84] S. Lany, A. Zunger, *Model. Simul. Mat. Sci. Eng.* **2009**, *17*, 084002.
[85] H.-P. Komsa, T. T. Rantala, A. Pasquarello, *Phys. Rev. B* **2012**, *86*, 045112.
[86] R. J. Bell, P. Dean, *Discuss. Faraday Soc.* **1970**, *50*, 55.
[87] J. Dong, D. A. Drabold, *Phys. Rev. B* **1996**, *54*, 10284.
[88] M. Unge, T. Christen, *Chem. Phys. Lett.* **2014**, *613*, 15.
[89] Y. Youn, Y. Kang, S. Han, *Comp. Mat. Sci.* **2014**, *95*, 256.
[90] T. M. Chang, J. D. Bauer, J. L. Skinner, *J. of Chem. Phys.* **1990**, *93*, 8973.
[91] W. Humphrey, A. Dalke, K. Schulten, *J. Mol. Graph.* **1996**, *14*, 33.
[92] K. Jarolimek, R. A. de Groot, G. A. de Wijs, M. Zeman, *Phys. Rev. B* **2010**, *82*, 20.
[93] C. A. Tolman, *Chem. Rev.* **1977**, *77*, 313.
[94] R. P. Vedula, N. L. Anderson, A. Strachan, *Phys. Rev. B* **2012**, *85*, 205209.
[95] H. Toraya, *J. Appl. Crystallogr.* **2000**, *33*, 95.
[96] J. Schmidt, F. M. Schuurmans, W. C. Sinke, S. W. Glunz, A. G. Aberle, *Appl. Phys. Lett.* **1997**, *71*, 252.
[97] V. Gritsenko, S. Nekrashevich, V. Vasilev, A. Shaposhnikov, *Microelectron. Eng.* **2009**, *86*, 1866.
[98] K. Midya, S. Dhar, A. Kottantharayil, *J. Appl. Phys.* **2013**, *114*, 154101.
[99] Y. N. Novikov, V. A. Gritsenko, *Journal of Non-Crystalline Solids* **2020**, *544*, 120186.
[100] T. H. Kim, I. H. Park, J. D. Lee, H. C. Shin, B.-G. Park, *Appl. Phys. Lett.* **2006**, *89*, 063508.
[101] A. Sanjoh, N. Ikeda, K. Komaki, A. Shintani, *J. Electrochem. Soc.* **1990**, *137*, 2974.
[102] R. Solanki, A. Manwani, A. Mahajan, R. M. Patrikar, *Superlattices and Microstruct.* **2020**, *144*, 106577.
[103] J.-Y. Sung, J.-k. Jeong, K.-R. Nam, G.-W. Lee, *Trans. Electr. Electron. Mater.* **2021**, *22*, 432.